ADVANCED MATERIALS
www.advmat.de

Enhancing Electron Correlation at a 3d Ferromagnetic Surface

David Maximilian Janas, Andrea Droghetti, Stefano Ponzoni, Iulia Cojocariu, Matteo Jugovac, Vitaliy Feyer, Miloš M. Radonjić, Ivan Rungger, Liviu Chioncel, Giovanni Zamborlini,* and Mirko Cinchetti*

Spin-resolved momentum microscopy and theoretical calculations are combined beyond the one-electron approximation to unveil the spin-dependent electronic structure of the interface formed between iron (Fe) and an ordered oxygen (O) atomic layer, and an adsorbate-induced enhancement of electronic correlations is found. It is demonstrated that this enhancement is responsible for a drastic narrowing of the Fe d-bands close to the Fermi energy (E_F) and a reduction of the exchange splitting, which is not accounted for in the Stoner picture of ferromagnetism. In addition, correlation leads to a significant spin-dependent broadening of the electronic bands at higher binding energies and their merging with satellite features, which are manifestations of a pure many-electron behavior. Overall, adatom adsorption can be used to vary the material parameters of transition metal surfaces to access different intermediate electronic correlated regimes, which will otherwise not be accessible. The results show that the concepts developed to understand the physics and chemistry of adsorbate–metal interfaces, relevant for a variety of research areas, from spintronics to catalysis, need to be reconsidered with many-particle effects being of utmost importance. These may affect chemisorption energy, spin transport, magnetic order, and even play a key role in the emergence of ferromagnetism at interfaces between non-magnetic systems.

1. Introduction

The adsorption of non-magnetic atoms and molecules on a ferromagnetic (FM) transition metal surface creates a hybrid interface exhibiting a plethora of novel exotic physical phenomena.[1] On the one hand, the adsorbate orbitals become spin-polarized because of the contact with the ferromagnet,[2] resulting in an induced spin polarization that can be measured in nano-scale tunnel magnetoresistance experiments.[3–5] On the other hand, many magnetic properties of the transition metal surface are drastically modified. For example, in ultrathin FM films, CO, fullerene and other molecules enable the steering of the magnetization direction.[6,7] The adsorption of a π-conjugated organic molecule on a ferromagnetic substrate locally increases the strength of the magnetic exchange interaction between its underlying magnetic atoms, thus leading to magnetic hardening.[8,9] Chemisorption of oxygen on Fe induces a strong Dzyaloshinskii–Moriya interaction,[10] while a

D. M. Janas, S. Ponzoni, G. Zamborlini, M. Cinchetti
TU Dortmund University
Department of Physics
44227 Dortmund, Germany
E-mail: giovanni.zamborlini@tu-dortmund.de

A. Droghetti
School of Physics & CRANN
Trinity College
Dublin D02 PN40, Ireland
E-mail: andrea.droghetti@tcd.ie

The ORCID identification number(s) for the author(s) of this article can be found under https://doi.org/10.1002/adma.202205698.

DOI: 10.1002/adma.202205698

I. Cojocariu, M. Jugovac, V. Feyer
Peter Grünberg Institute (PGI-6)
Forschungszentrum Jülich GmbH
52428 Jülich, Germany

M. M. Radonjić
Institute of Physics Belgrade
University of Belgrade
Pregrevica 118, Belgrade 11080, Serbia

I. Rungger
National Physical Laboratory
Teddington TW11 0LW, UK

L. Chioncel
Theoretical Physics III
Center for Electronic Correlations and Magnetism
Institute of Physics and Augsburg Center for Innovative Technologies
University of Augsburg
86159 Augsburg, Germany

hydrogenated Fe double layer on an Ir(111) substrate supports the formation of magnetic skyrmions.[11] For selected interfaces, large molecules can surprisingly lead to a ferromagnetic response in otherwise non-magnetic nanostructures.[12] For all these phenomena, the main driving mechanism behind the emergent spin properties is the hybridization between the orbitals of the adsorbate and the 3d electronic bands of the surface. However, the complex interplay between the change in the local spin-dependent electronic structure of the metal surface layers and the emergent adsorbate spin-polarization is not yet fully understood.

Most research works to date (for example, refs. [2,12–14]) describe adsorbates on ferromagnets in terms of an effective single-particle Stoner picture[15] derived from density functional theory (DFT).[16–18] This explains ferromagnetism in 3d transition metals (Ni, Fe, Co) and their alloys as resulting from a rigid energy shift (the so-called exchange splitting) of the majority and minority 3d-bands under the influence of the exchange interaction treated in a static mean-field approximation. However, FM transition metals are rather correlated[19,20] as the open 3d shells are tightly bound to the ionic cores, which crucially affects their electronic and magnetic properties and makes single-particle approximations inaccurate.[21–23] Specifically, electron correlation leads to the narrowing of the 3d bandwidth and the reduction of the exchange splitting[24–29] sometimes accompanied by intrinsic many-body features, called satellites, at high binding energy in excitation spectra.[30] All these effects are likely to be modified upon chemisorption of atomic and molecular adsorbates, but this intriguing physics has not been thoroughly investigated. To the best of our knowledge, even the most basic question on whether adsorption enhances or reduces electron correlation has never been posed in explicit terms. Here we are aiming to start filling this knowledge gap.

To demonstrate how adsorption alters electron correlation and thereby affects the electronic and magnetic structure of interfaces, we consider, as a model system, chemisorbed oxygen atoms atop FM iron forming a p(1 × 1)O–Fe(100) reconstruction. Besides its interest for such fundamental electronic structure problems, this system is also important for applications, as it is widely used for highly efficient spin detection in electron spectrometers.[31–33] We provide the direct proof that the oxygen adsorption drastically enhances electron correlation at the surface, leading to the breaking down of the Stoner-like picture of band ferromagnetism. In particular, we find that hybrid O–Fe states become extremely narrow and localized in energy in a 1 eV range below the Fermi level, reducing, at the same time, the exchange splitting. Furthermore, strongly spin-polarized adsorbate–FM satellite features appear in the excitation spectra at low binding energies. Overall, the system is in a unique intermediate metallic correlated regime between ferromagnetic metals and strongly correlated transition metal oxides.

Our observations have been possible thanks to the recent integration of imaging spin-filters with a new generation of photoemission electron microscopes (PEEMs) enabling the parallel acquisition of momentum- and spin-resolved photoelectron distributions within the same experiment (spin-resolved momentum microscopy).[34] The results are interpreted using a state-of-the-art theoretical method, which includes correlation effects beyond DFT overcoming the limitation of the effective single-particle DFT picture.

2. Results

2.1. DFT Versus DFT+DMFT

In order to rationalize the basic electronic structure of interfaces formed by adsorbates on FM surfaces, at first, we consider the d-band model introduced by Hammer and Nørskov, which is widely used to understand and predict the catalytic activity of transition metal surfaces.[35–37] According to this single-particle model, hybridization may occur when an atom or molecule is bound in the vicinity of the surface. In particular, the adsorption takes place through two consecutive steps. The first includes the interaction of a molecular state with the delocalized, broad metal sp-band. As deduced by Newns in 1968,[38] the coupling causes the molecular state to shift and to broaden in energy into a resonance, as its lifetime is reduced due to possible relaxation into the metal band. In the second step, that resonance interacts with the narrow d-band of the metal surface, which acts similarly to a discrete atomic level located at the band center and splits the molecular state into a bonding and an antibonding resonance. At a ferromagnetic surface, this splitting occurs spin-dependently, and thus, hybridization induces an exchange splitting on the emerging adsorbate resonances,[39] as depicted by the single-particle picture in **Figure 1**a (left). The position of the bonding and antibonding resonances with respect to the Fermi energy determines the strength of the chemisorption, and moreover, the change in the filling of the *d* band.

This rationalization can already be grasped in electronic structure calculations performed by means of spin-polarized DFT, which we consider as an effective single-particle theory. The resulting density of states (DOS) of the Fe(100) and p(1 × 1) O–Fe(100) systems are reported in Figure 1b and projected, for both majority and minority spin channels, over the surface Fe atom (black curve) and the O adatom (red and blue curves). Qualitatively, we can immediately appreciate the basic physics described by the d-band model. In Fe(100), the majority d-band is almost entirely filled and the band structure is spin-split according to the Stoner-like picture of band ferromagnetism. After oxygen adsorption, the formation of the O–Fe bonding state with mostly O character appears in the majority spin channel between −9 and −5 eV below the Fermi energy , whereas the minority states are centered between −8 and −4 eV. In contrast, the antibonding states with mostly Fe character are rather close to or above E_F. The orbital-resolved DOS is presented in Section S1, Supporting Information. In the minority channel, the system tends to become more insulating with the DOS that is reduced around E_F, while a fraction of electrons (≈0.17*e*) is moved from the d_{xy} and d_{z^2} orbitals to other orbitals. On the other hand, in the majority channel, the d states, in particular the d_{xy}, which are strongly hybridized with the O p_x and p_y orbitals, are dragged toward E_F. Although the calculated reduction in the majority d_{xy} state occupation is only 0.1 electrons, as we will see in the following, this effect is one of the ingredients that enhance electron correlations, since it enables

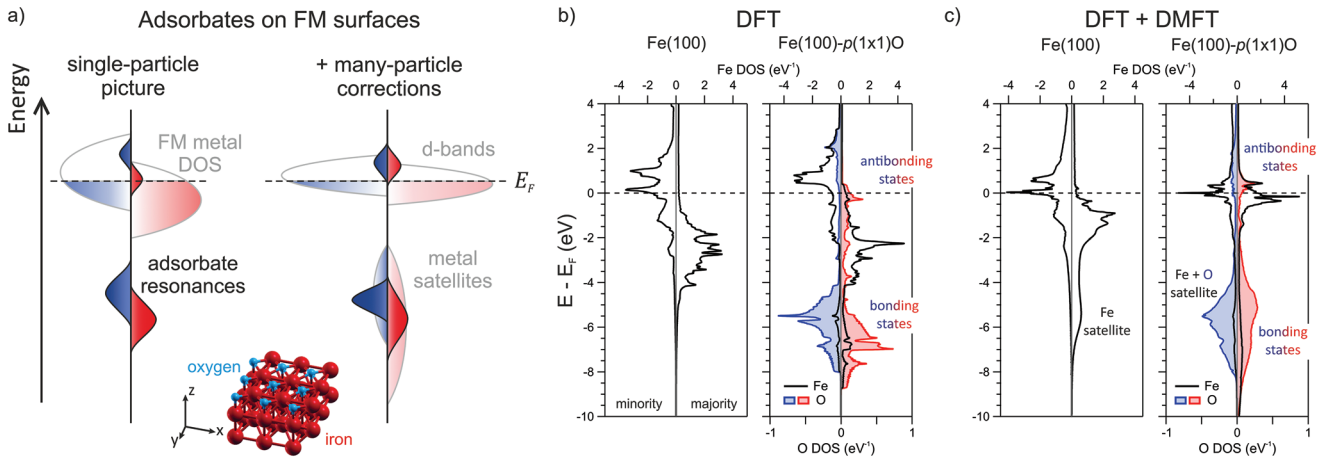

Figure 1. a) Scheme of the DOS for adsorbed atoms or molecules hybridized with FM surfaces. The left side depicts the typical result of the d-band center model (single-particle model) comprising the spin-dependent splitting of the atomic oxygen states into antibonding and bonding resonances (black lines). In this model the metal DOS (grey lines) is almost unaffected by the O adsorption. Including electron correlation (right panel) drastically changes the metal DOS, unveiling the emergence of satellites at higher binding energies and a severe reduction of the exchange splitting close to Fermi. b,c) DOS for the Fe(100) and Fe(100)–p(1 × 1)O surfaces projected on the surface Fe atom (and O atom) calculated with DFT (b) and with DFT + DMFT (c), respectively.

three-body scattering processes between d electrons and particle–hole pairs.[40]

Now we include correlation effects viathe so-called many-electron self-energy $\Sigma(E)$, which describes the potential felt by the electrons because of their interaction beyond the effective single-particle picture of the spin-polarized DFT. In particular, $\Sigma(E)$ is calculated here by using dynamical mean field theory (DMFT)[41] with a solver that includes all second-order terms in the effective electron–electron interaction U and Hund's coupling J between Fe 3d electrons[40,42] (for further details see Experimental Section). DMFT neglects spatial fluctuations (i.e., the spatial correlation between electrons on different atoms), but considers temporal (i.e., dynamical) fluctuations due to electron correlations, and the self-energy is therefore energy-(or frequency-) dependent. The method was shown to describe the physics of transition metals[19,27] and our implementation has proven accurate in reproducing correlation-related features in photoemission spectra of transition metal thin films.[40] In our calculations, the interaction parameters U and J are used as empirical parameters that are fixed by comparing the theoretical and the experimental spectra. The resulting DOS for both Fe(100) and p(1 × 1)O–Fe(100) are shown in Figure 1c.

At the clean Fe(100) surface, correlation shifts the states toward the Fermi energy leading to a noticeable reduction of the exchange splitting between the majority and the minority *d*-bands accompanied by the narrowing of the majority d-band compared to the single-particle DFT picture. Furthermore, a pronounced satellite feature for majority electrons appears centered at about −5 eV. The considered U and J are respectively equal to 1.8 and 0.5 eV, and they are within the range of values that were used in previous studies.[22] Notably, correlation effects appear much more pronounced for the majority than for the minority d-band. The physical picture can be easily understood considering that in a FM metal, electrons propagate through the Stoner mean-field created by electrons of opposite spin. The self-energy dynamical contribution added to the system describes scattering of single electrons against the Fermi sea creating particle–hole pairs. In a strong ferromagnet like the Fe surface studied here, the majority band is not entirely filled and, close to the Fermi energy, its contribution to the DOS is small. In contrast, the minority DOS near the Fermi energy is large. Thus, for any process involving particle–hole pair creation, the pair is more likely to appear in the minority band. Majority-spin electrons will scatter minority-spin pairs, with effective interaction U, whereas minority-spin electrons scatter minority-spin pairs with a lower effective interaction is $U - J < U$. As a result, majority spin electrons are more correlated than minority spin electrons. These are well-established results, which were predicted by early DFT+DMFT calculations and supported by experiments.[26,27,43]

Crucially, the overall physical picture changes for p(1 × 1)O–Fe(100). The U and J values of the Fe surface atoms used in our DMFT calculations for the p(1 × 1)O–Fe(100) interface need to be increased to U = 3.0 eV and J = 1.1 eV to account for the experimental spectral properties presented in the next section. The DOS of p(1 × 1)O–Fe(100) calculated with the same U = 1.8 eV and J = 0.5 eV as for Fe(100) is presented in Section S2, Supporting Information highlighting the deficiency of the results for those smaller parameters. This finding suggests that the electron–electron interaction becomes effectively less screened after oxygen adsorption. The quite large U of Fe is the key ingredient leading to enhanced electronic correlation due to oxygen adsorption. In fact, the importance of correlation effects for d electrons in transition metals is primarily determined by the strength of the effective electron–electron interaction U relative to the band width. As mentioned earlier, the other factor affecting electron correlation is the band filling. In the extreme case of a fully filled band, no electron–hole pairs can be created, and correlation effects would be absent irrespective of U. Instead, when a band becomes partially filled, correlation is activated. The relation between band filling and correlation is further discussed in

Section S3, Supporting Information. The value of the on-site energy of the atomic levels with respect to the energy of the d-band controls the spin-dependent occupation of the surface Fe d orbitals, and with that, the strength of electron correlation and the consequent changes in the electronic structure. We generally find that the system becomes more (less) correlated for a large (small) adsorbate on-site energy when the number of electrons of the majority d orbitals, and in particular of the d_{xy} orbital, is reduced away from (increased toward) full occupancy, while the minority d orbitals are overall filled (emptied) with respect to the case of the clean Fe surface. This indicates that an adsorbate can effectively be used to tune electron correlation effects at metallic surfaces. According to our DFT calculation, since the p(1 × 1)O–Fe(100) surface presents 0.1 holes in an otherwise almost filled majority 3d orbitals, it can be considered in a regime of relatively high correlation. This fact, together with the discussed U enhancement, is enough to drive dramatic changes in the electronic structure: the exchange splitting is quenched, and the d-band becomes narrower than in the clean surface because of the larger U. Comparing the results for p(1 × 1)O–Fe(100) in Figure 1b,c, we see that also the minority d-band, and not just its majority counterpart, becomes renormalized by correlation. Interestingly, while correlation does not change the charge of the surface Fe atom d shell occupation (6.8 e), it strongly reduces their magnetic moment from 3 to 1.8 μ_B. Besides that, we note that the enhanced correlation in the minority d-band also leads to the formation of a minority satellite feature, which was absent in Fe(100). These findings are rationalized in Figure 1a (right).

The change in the electron correlation can be quantitatively evaluated through the mass enhancement factor m^*/m, which is the ratio between the effective mass m^* of surface d orbitals including electron correlation and the effective mass m in the single-particle picture. The mass enhancement measures how much d-electrons effectively become heavier because of correlation. For uncorrelated electrons m^*/m would be equal to 1. In Fe(100) we find an average mass enhancement for surface d orbitals equal to 1.23 (spin up) and 1.36 (spin down) (the results resolved for each orbital are presented in Section S4, Supporting Information). The surface is weakly correlated. After oxygen adsorption, the average m^*/m increases up to 1.52 (spin up) and 1.43 (spin down). The system, therefore, becomes medium correlated. In particular, the largest mass enhancement (1.60) is found for the surface spin up Fe d_{xy} orbital, which, as stated above, is hybridized with the O p_x and p_y states and slightly hole-doped. This confirms that the formation of metal–adsorbate bond strongly affects the electron correlation. Adsorbates can effectively be used to vary the material parameters accessing intermediate metallic correlated regimes rather different from that of pristine ferromagnetic surfaces.

2.2. Spin-Integrated Band Structure of the Interface

Now that electron correlation effects have been introduced from the theoretical point of view, we will investigate how they manifest in experiments. We obtain the p(1 × 1)O–Fe(100) surface by exposing a bare iron substrate to oxygen and we employ angle-resolved photoelectron spectroscopy to access the electronic structure of the system under study (see Experimental Section). We start by comparing the so-called momentum maps (i.e.,, the photoelectron distribution as a function of the electron parallel momentum) taken at the Fermi level before and after exposing the clean iron sample to O_2. The corresponding momentum maps are reported in **Figure 2**a,b, respectively. For guidance, the first surface Brillouin zone (SBZ) is sketched (gray square) alongside the high-symmetry lines connecting the $\overline{\Gamma}$, $\overline{X}$, and $\overline{M}$ points (red lines). The surface normal is assumed along the Cartesian z-axis. Both incidence plane of

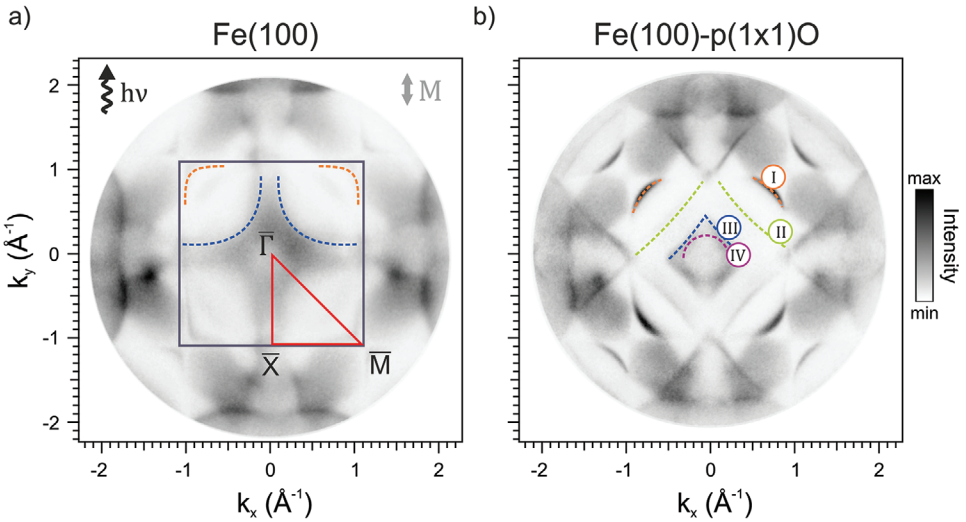

Figure 2. a,b) Momentum maps at E_F for the clean Fe(100) (a) and passivated Fe(100)–p(1×1)O (b) surface. In (a) the surface Brillouin zone of the two systems is indicated by a gray square and red lines mark the high-symmetry lines. The direction of the incidence light beam (impinging at 66° with respect to the surface normal) and the magnetization M lie parallel to the k_y-direction. Comparing the two images reveals the emergence of additional states that originate from the hybridization between iron substrate and oxygen overlayer. The maps were acquired using p-polarized light with photon energy $h\nu = 64$ eV.

the photon beam and magnetization direction lie parallel to the k_y-direction as indicated by the black and the gray arrow, respectively.

For pristine Fe(100) two prominent features can be observed within the SBZ that are closely related to the d_{xz}, d_{yz} states of bulk iron.[44–46] The first one extends along the $\overline{\Gamma X}$ path (blue), and vanishes near $\overline{\Gamma}$ and $\overline{X}$. The second one is along the $\overline{\Gamma M}$ path and located close to the $\overline{M}$-point (orange). As already observed in previous studies, the passivation with oxygen leads to the formation of the Fe(100)–p(1×1)O phase, which shows remarkable changes in the electronic structure.[47] The corresponding momentum map is shown in Figure 2b. Compared to the clean surface, the state along $\overline{\Gamma X}$ is replaced by a diamond-like shaped state close to $\overline{\Gamma}$ (blue) together with a ring-shaped one in the center of the SBZ (violet), while the feature near $\overline{M}$ (orange) becomes rounder and more intense. Furthermore, another diamond-shaped state arises that connects the four $\overline{X}$-points (green). Notably, all these states appear much sharper and more prominent than the ones for the clean Fe(100) surface. The enhancement can be directly related to the dramatic narrowing of the *d*-bands caused by the larger electron correlation.

The changes in the electronic structure can be further appreciated by observing the energy dispersion of the marked features along the symmetry directions indicated in Figure 2a. The resulting plot is shown in **Figure 3**a, where we also highlight the electronic orbital nature of the states related to the Fe(100)–p(1×1)O surface. Their surface nature was established by comparing photoemission measurements taken at different photon energies (further details are given in Section S5, Supporting Information. Those states close to the Fermi level are all antibonding states formed between the antibonding O p- and the Fe d-orbitals, but, in contrast to the bonding states at –6 eV, their main contribution stems from the Fe d-orbitals. They are, therefore, quasiparticle states, which means single-particle-like electronic states, but renormalized by interaction effects. They extend over a narrow energy region about 1 eV width and their flatter energy dispersion compared to quasiparticles states of the clean Fe is a consequence of enhanced correlation as discussed above. The photoemission data can in fact be compared to the momentum-resolved DOS of Figure 3b calculated with DFT+DMFT (a comparison of ARPES data and DMF T for Fe(100) is reported in Section S6, Supporting Information). The agreement between theory and measurements is remarkably good with the position and dispersion of most features, which appear quantitatively consistent. We note that, in contrast, the momentum-resolved DOS calculated by DFT without including the many-electron self-energy completely fails to match the photoemission data, and a similar failure is also found when using "static" corrections for DFT designed to account for insulating behaviors in oxides (see Section S7, Supporting Information). This is because the system is an intermediate correlated metal and only dynamical self-energy contributions can capture the correct physics. The narrowing of the electronic bands found in experiments for Fe(100)–p(1×1)O reflects the enhancement of the m^*/m ratio induced by the stronger electron–electron correlation. Previous studies already speculated that the mismatch between the experimental results and the DFT calculations might be due to electron correlations[48] and first attempts to implement many-body corrections were performed.[32] However, the full magnitude of many-body effects was not captured, and thus, it was not possible to establish a conclusive model conceiving the physics occurring at the chemisorbed interface. Here we provide the first direct evidence of enhancement of electron correlation induced by the oxygen adsorption.

We now focus on the bands at higher binding energy centered at –6 eV. We identify three parabolic dispersing states along the $\overline{XM}$-path (Figure 3a). They unambiguously stem from the bonding states between the 2p (p_x, p_y, p_z) orbitals of the oxygen and the d orbitals of the metal[49,50] (see Figures S10 and S11 in Section S8, Supporting Information, for the orbital-resolved spectral functions). Yet, the most striking feature in this energy region is the merging of the sharp bonding states into the broad satellite feature of iron. This satellite appears as a diffuse background in the region from –5.0 to –7.0 eV, near the $\overline{\Gamma}$-point (Figure 3a) and it can be clearly identified also in the total density of states (see Figure 1c). This is a many-body feature, which is absent in a single-particle band structure description, and which is enhanced through the oxygen adsorption because of the strengthening of the effective electron-electron interaction *U*.

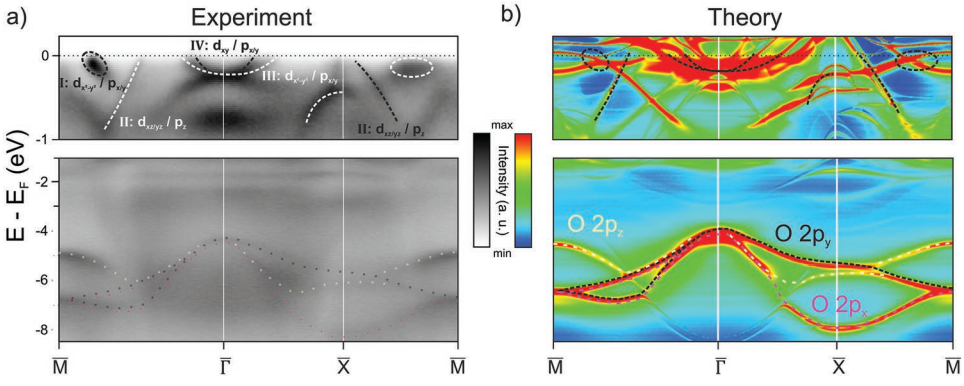

Figure 3. a,b) The surface band structure for the Fe(100)–p(1×1)O interface along the $\overline{M}$ – $\overline{\Gamma}$ – $\overline{X}$ – $\overline{M}$ direction, determined by momentum-resolved photoemission measurements using a photon energy of $h\nu = 64$ eV (a), and calculated including electron correlation via the self-energy (b). The upper panels in (a) and (b) depict the band structure in an energy range from E_F to –1.0 eV, while the two bottom panels show the sections from –1.0 to –8.5 eV.

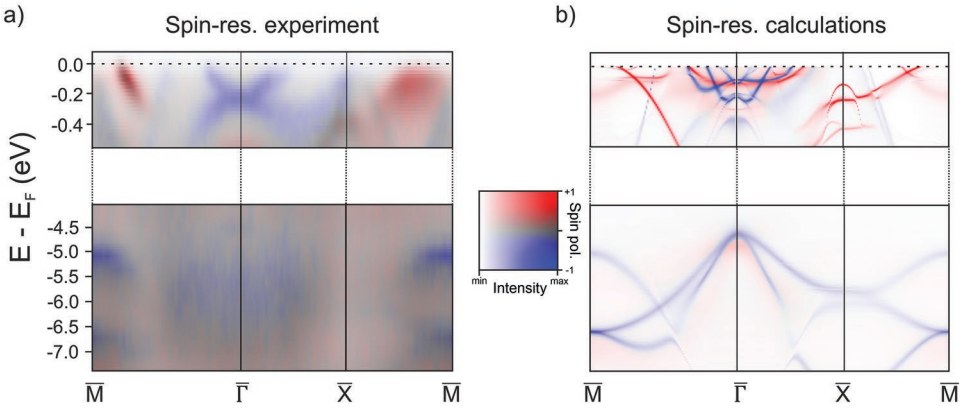

Figure 4. a) Experimentally measured spin-resolved band structure of the Fe(100)–p(1×1)O surface taken at $h\nu = 64$, with the corresponding 2D color scale where blue indicates minority and red majority states. The experimental data cover the energy sections of the antibonding states from E_F to –0.5 eV (top panel) and of the bonding states from –4.0 to –7.5 eV (lower panel). A 2D spin- and momentum-resolved photoemission map for Fe(100)–p(1×1)O can be found in Figure S7, Supporting Information. b) The theoretically derived spin-polarized band structure is depicted for the same energetic range as (a).

2.3. Spin-Resolved Band Structure of the Oxygen-Passivated Fe Surface

After having assigned the main features of the surface band structure, we now analyze the spin-resolved photoemission data, which are shown in **Figure 4**a. These allow us to track the dispersion of the antibonding and bonding states in the two spin channels. To visualize both the intensity and the spin-polarization within the same plot, the color scale becomes a 2D map like the one depicted in Figure 4a. From these data, we can immediately extrapolate the spin character of the earlier reported antibonding states near the Fermi level. While the states close to the center of the SBZ stem mainly from the minority electrons (blue), the one located near the $\overline{\text{M}}$-point has a strong majority character (red).

For a one-to-one comparison, the spin-resolved theoretical results are placed side-by-side in Figure 4b. As mentioned at the beginning, it is in the spin-resolved spectra, where the severe consequences of the enhanced electron correlation can be better appreciated. The first one is the breaking down of the single-particle Stoner-like picture of ferromagnetism in the region close to the Fermi energy, where there is no evidence of the expected exchange split 3d-bands. Although there are some differences between the theoretical and the experimental results near the $\overline{\Gamma}$-point possibly due to matrix element effects or to DMFT neglecting non-local correlation,[51] the theoretical and experimental picture are qualitatively consistent, and the agreement is overall good for other points in the SBZ. Importantly, the overall reduced exchange splitting of the d-bands due to oxygen does not manifest by a suppressed spin-polarization of the states at the Fermi level. Therefore, in previous publications (see for example ref. [49]) it was assumed that the d-bands remain mostly unaffected, which was in agreement with computational predictions at the time that were based on single-particle approximations. The comparison with previous works further highlights the importance of our work, since only state-of-the-art spin-resolved ARPES experiment compared to state-of-the-art calculations can disentangle and correctly identify the complex features in the spin-resolved band structure of the Fe–O system. This is also true for the region from –4 to –8 eV, where at first glance the experimental spectra seem fully spin-polarized, while the theoretical calculations indicate that the minority resonances are sharper, and the majority bands are significantly broadened.

To single out this effect in the experimental data, the two spin contributions can be viewed separately. The corresponding spin channels are reported in **Figure 5**. The energy broadening and the exchange splitting are quantified by extracting intensity profiles along the energy axis from the graph and by fitting the resulting spectra with a Gaussian function. The energy and momentum ranges are delimited by dotted boxes. The extracted peak position is superimposed to the data (red and blue triangles), while the broadening is assumed to be the FWHM of the corresponding Gaussian. Strikingly, these results demonstrate the collapse of the exchange splitting close to the Fermi level. In fact, the exchange splitting appears even slightly reversed as we measure the minority states $\Delta_{E_F,\overline{\Gamma}} = -(40 \pm 10)$ meV lower in energy. In addition, the broadening of the majority state is enhanced at $\overline{\Gamma}$, where it amounts to $w_{E_F,\uparrow} = (250 \pm 20)$ meV compared to $w_{E_F,\downarrow} = (180 \pm 20)$ meV for the minority states. The same trend is observed near $\overline{\text{M}}$, although here the change is subtler and appears to increase when moving toward $\overline{\Gamma}$ (see Section S9, Supporting Information, for the full overview). Next, we discuss the results for the bonding oxygen 2p states, where, contrary to the findings at the Fermi level, an exchange splitting is still present.[49,50,52] For the $p_{x,y}$ states close to the $\overline{\Gamma}$-point we observe a splitting of $\Delta_{O_{2p},\overline{\Gamma}} = (360 \pm 30)$ meV and for the p_z states of $\Delta_{O_{2p},\overline{\text{M}}} = (230 \pm 50)$ meV near the $\overline{\text{M}}$-point. These results are in good agreement with the previous ones by Getzlaff et al. and Johnson et al.,[50,52] which are also based on spin- and angle-resolved photoemission data. Notably, toward $\overline{\Gamma}$, the p_z bands broaden into resonances that overlap with the iron satellites and therefore the two contributions cannot be disentangled (see Section S8, Supporting Information, for more details). As shown by the calculations presented in Figure 1c, this broad and spin-polarized resonance arises due to many-body interactions and was therefore not present in previous single-particle based calculations. Generally, the measured $\Delta_{O_{2p}}$

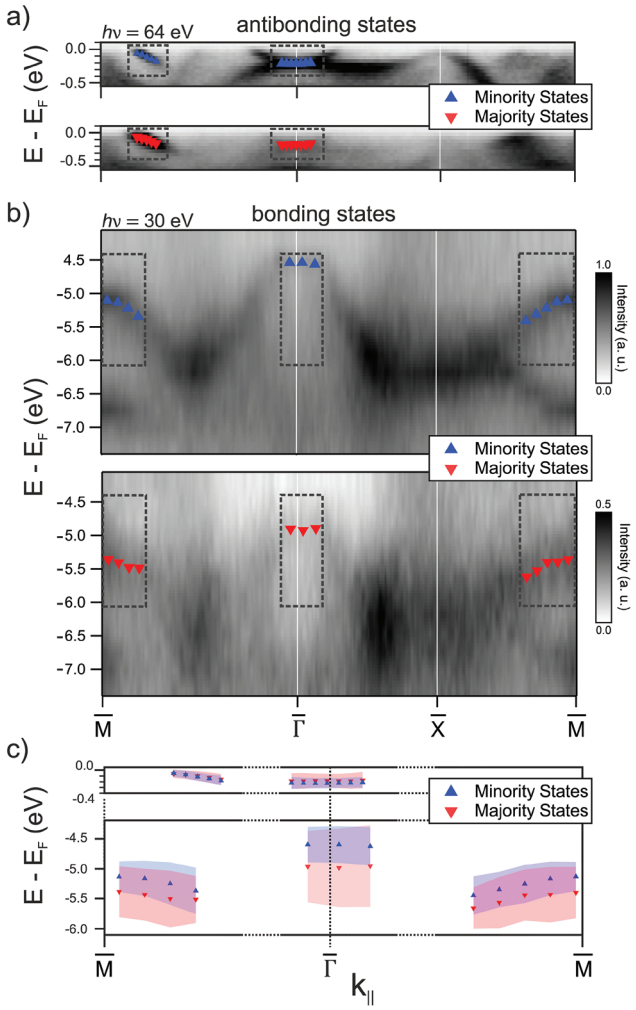

Figure 5. a,b) The separated majority and minority photoemission intensities for the antibonding Fe–O states (a) and bonding states (b) are displayed in the bottom and top panels, respectively. In (a) and (b) the blue and red triangles resemble the peak positions of Gaussian fits that were performed for line profiles along the energy axis within the highlighting boxes. c) Both fitting results are displayed mutually, including also the widths of the determined Gaussians. To maximize the signal for the analysis, the antibonding states presented here were recorded using a photon energy of $h\nu = 64$ eV, while the bonding states were probed at $h\nu = 30$ eV.

is considerably smaller than the exchange splitting of about 1.5 eV that can be estimated from the DFT Stoner-like picture and the DOS reported in Figure 1a. This difference is the result of electron correlations. Besides drastically reducing the exchange splitting, electron correlation also makes the broadening, i.e., the inverse lifetime, strongly spin-dependent. Consequently, we see a strong enhancement of the broadening that considerably smears out the majority features. At $\overline{\Gamma}$ the estimated width of the band is $w_{O_{2p},\overline{\Gamma},\uparrow} = (640 \pm 50)$ meV for the majority band in comparison to $w_{O_{2p},\overline{\Gamma},\downarrow} = (310 \pm 20)$ meV for the minority one. In accordance, the same behavior is found for the states close to $\overline{M}$. We remind that the electrons' lifetime in this energy region is related to the damping into the Fe satellite. This satellite is much more prominent in the majority channel than in the minority. Therefore, majority electrons relax faster than minority ones. This is an example of dynamic spin-filtering[53] driven by electron correlation.

3. Conclusion

In the study of atomic adsorption on transition metals, the adsorbate-induced changes in the DOS of the metal are generally considered as an insignificant perturbation compared to the metal-induced changes on the adsorbate state.[54] Our work shows that this is clearly not the case for ferromagnetic metallic surfaces. The chemical bond between the adsorbate and the metal can enhance correlation effects and, as consequence, it can drive dramatic changes in the electronic structure, spin-polarization, and magnetic moment. This phenomenon was here analyzed in great detail for the p(1×1)O–Fe(100) interface and carefully verified experimentally.

Based on our results, we propose that the adsorption of atoms or small molecules makes possible the realization of intermediate correlated metallic regimes, which would otherwise not be found in any other material systems. Furthermore, concepts developed to understand the physics and chemistry of adsorbate–FM metal interfaces, as the d-band center model, eventually need to be reconsidered with many-particle effects being of utmost importance. Correlation may affect chemisorption energy, transport or also play a key role in stabilizing magnetic order or even in the emergence of ferromagnetism at various molecular interfaces, such as C_{60}/Cu.[12]

4. Experimental Section

Sample Preparation: For preparing the iron film, a MgO(100) crystal was cleaned in vacuum by two cycles of ion sputtering at 2 keV Ar^+ and subsequent annealing at 870 K for 45 min.[55] Afterward, a 300 nm thick Fe(100) film was epitaxially grown in situ by e-beam deposition on the clean MgO. This preparation ensures an in-plane magnetization direction lying along the Fe [001] axis. The resulting surface was cleaned in the experimental chamber through cycles of ion sputtering (typically 0.5 keV Ar^+) and annealing (up to 870 K). The Fe(10)–p(1 × 1)O was prepared by passivating the Fe surface through O_2 exposure (30 L) while the sample was kept at ≈820 K. After closing the O_2, the interface was annealed to870 K for 5 min, removing excess oxygen and obtaining the desired reconstruction.

Angle-Resolved Photoelectron Spectroscopy: The momentum-resolved photoemission was performed using a PEEM microscope in momentum operation mode which is installed at the NanoESCA beamline of the Elettra synchrotron in Trieste (Italy). The microscope is equipped with a W(001)-based spin detector,[56] which enables collecting constant energy spin-resolved maps within the entire Brillouin zone of the system. The photon beam impinges under an angle of 24° with respect to the sample surface and along the $k_x = 0$ line. The analysis of the spin-resolved images was performed following the procedure described.[57] Before each measurement, the Fe sample was remanently magnetized along the Fe[001] direction using an oriented permanent magnet, which was brought close to the sample surface in the analysis chamber.

Electronic Structure Calculations: Electronic structure calculations were performed by using the Green's function-based code Smeagol,[58,59] which obtained the Kohn–Sham DFT Hamiltonian from the DFT package Siesta.[60] The system was described as a surface region comprising eight Fe layers plus eventually one O atom in contact with a semi-infinite bulk Fe substrate. Details on how the partitioning was implemented can be found in ref. [40], while the embedding function

describing the electronic coupling between the surface region and the substrate is calculated using the algorithm in ref. [61]. Core electrons were treated with norm-conserving Troullier–Martin pseudopotentials. The valence states were expanded through a numerical atomic orbital basis set including multiple-ζ and polarized functions.[60] The electronic temperature was set to 300 K. The real space mesh was set by an equivalent energy cutoff of 300 Ry. DFT calculations were carried out within the local spin density approximation (LSDA),[16,17] and considering a 21 × 21 *k*-point mesh to compute the self-consistent charge density. The photoemission simulations were then performed using that density matrix as input for a non-self-consistent calculation and plotting the *k*-dependent spectral function for 206 *k*-points along each high symmetry line in the SBZ. Matrix elements effects were neglected. DFT+DMFT calculations were carried out using the computational implementation described in refs. [40,42]. Second-order perturbation theory in the electron–electron interaction was employed as solver[42] allowing for the fast evaluation of the self-energy directly on the real energy axis with no need for any analytic continuation schemes. The downfolding of the system onto the correlated subspace of the Fe 3d orbitals, which were treated within DMFT, was achieved using the algorithm in ref. [62]. Only the first three out-most surface layers were considered as correlated to reduce the computational effort. It was checked that the inclusion of more correlated layers had no visible effect on the electronic structure of the first topmost surface layer. The general orbital-dependent Coulomb interaction parameters were considered in the calculations and expressed in terms of Slater integrals F_0, F_2, and F_4.[63] These were connected to the average effective Coulomb and exchange interactions, which were reported in the main text, through the relations $U = F_0$ and $J = (F_2 + F_4)/14$. The ratio F_4/F_2 was assumed to correspond to the atomic value of ≈0.625.[64] In the case of p(1 × 1)O–Fe(100), the *U* and *J* values of only the first topmost surface layer were varied to obtain a good agreement with the experimental results as described in the main text. The *U* and *J* for the second and third layer were instead fixed to 1.8 and 0.5 eV. All energies were shifted in such a way as to set the Fermi level at 0 eV. To calculate the second-order self-energy, an energy grid comprising 4400 points and extending from −16 to 6 eV was used. The surface region was optimized by DFT within the LSDA by means of a slab calculation using Siesta. The Fe lattice constant was fixed equal to experimental bulk value. The position of the atoms in bottom 4 layers were constrained, while the position of the Fe and O atoms in the topmost 4 layers were allowed to relax until the ionic forces were smaller than 0.01 eV Å^{-1}. The obtained structure was then attached to the semi-infinite bulk Fe substrate for the Smeagol DFT and DFT+DMFT calculations.

Supporting Information

Supporting Information is available from the Wiley Online Library or from the author.

Acknowledgements

M.C., G.Z., S.P., and D.M.J. acknowledge funding from the European Research Council (ERC) under the European Union's Horizon 2020 research and innovation programme (Grant Agreement No. 725767—hyControl). This paper was partly supported by EC H2020 programme under grant agreement No 965046, FET-Open project INTERFAST (Gated interfaces for fast information processing). The research leading to this result has been partially supported by the project CALIPSOplus under Grant Agreement 730872 from the EU Framework Programme for Research and Innovation HORIZON 2020. A.D. acknowledges funding by the Science Foundation Ireland (SFI) and the Royal Society through the University Research Fellowship URF-R1-191769. M.M.R. acknowledges funding provided by the Institute of Physics Belgrade, through the grant by the Ministry of Education, Science, and Technological Development of the Republic of Serbia. I.R. acknowledges the support of the UK government department for Business, Energy and Industrial Strategy through the UK National Quantum Technologies Programme. L.C. acknowledges the financial support by the Deutsche Forschungsgemeinschaft through TRR80 (project F6) Project number 107745057. Computational resources were provided by Trinity.

Open access funding enabled and organized by Projekt DEAL.

Note: The title of the article was corrected on January 19, 2023, after initial publication online: 3d was revised to indicate 3d-bands rather than three-dimensional.

Conflict of Interest

The authors declare no conflict of interest.

Data Availability Statement

The raw data that support the findings of this study are available in the ZENODO database, at https://zenodo.org/communities/interfast-fetopen.

Keywords

electron correlation, many-particle effects, spin filtering, Stoner model

Received: June 22, 2022
Revised: October 7, 2022
Published online: November 18, 2022

[1] M. Cinchetti, V. A. Dediu, L. E. Hueso, *Nat. Mater.* **2017**, *16*, 507.
[2] N. Atodiresei, J. Brede, P. Lazić, V. Caciuc, G. Hoffmann, R. Wiesendanger, S. Blügel, *Phys. Rev. Lett.* **2010**, *105*, 066601.
[3] C. Barraud, P. Seneor, R. Mattana, S. Fusil, K. Bouzehouane, C. Deranlot, P. Graziosi, L. Hueso, I. Bergenti, V. Dediu, F. Petroff, A. Fert, *Nat. Phys.* **2010**, *6*, 615.
[4] S. Schmaus, A. Bagrets, Y. Nahas, T. K. Yamada, A. Bork, M. Bowen, E. Beaurepaire, F. Evers, W. Wulfhekel, *Nat. Nanotechnol.* **2011**, *6*, 185.
[5] J. Brede, N. Atodiresei, S. Kuck, P. Lazić, V. Caciuc, Y. Morikawa, G. Hoffmann, S. Blügel, R. Wiesendanger, *Phys. Rev. Lett.* **2010**, *105*, 047204.
[6] K. Bairagi, A. Bellec, V. Repain, C. Chacon, Y. Girard, Y. Garreau, J. Lagoute, S. Rousset, R. Breitwieser, Y. C. Hu, Y. C. Chao, W. W. Pai, D. Li, A. Smogunov, C. Barreteau, *Phys. Rev. Lett.* **2015**, *114*, 247203.
[7] A. Quesada, G. Chen, A. T. N'Diaye, P. Wang, Y. Z. Wu, A. K. Schmid, *J. Mater. Chem. C* **2021**, *9*, 2801.
[8] M. Callsen, V. Caciuc, N. Kiselev, N. Atodiresei, S. Blügel, *Phys. Rev. Lett.* **2013**, *111*, 106805.
[9] K. V. Raman, A. M. Kamerbeek, A. Mukherjee, N. Atodiresei, T. K. Sen, P. Lazić, V. Caciuc, R. Michel, D. Stalke, S. K. Mandal, S. Blügel, M. Münzenberg, J. S. Moodera, *Nature* **2013**, *493*, 509.
[10] G. Chen, A. Mascaraque, H. Jia, B. Zimmermann, M. Robertson, R. Lo Conte, M. Hoffmann, M. A. G. Barrio, H. Ding, R. Wiesendanger, E. G. Michel, S. Blügel, A. K. Schmid, K. Liu, *Sci. Adv.* **2020**, *6*, eaba4924.
[11] P. J. Hsu, L. Rózsa, A. Finco, L. Schmidt, K. Palotás, E. Vedmedenko, L. Udvardi, L. Szunyogh, A. Kubetzka, K. Von Bergmann, R. Wiesendanger, *Nat. Commun.* **2018**, *9*, 1571.
[12] F. Al Ma'Mari, T. Moorsom, G. Teobaldi, W. Deacon, T. Prokscha, H. Luetkens, S. Lee, G. E. Sterbinsky, D. A. Arena, D. A. Maclaren, M. Flokstra, M. Ali, M. C. Wheeler, G. Burnell, B. J. Hickey, O. Cespedes, *Nature* **2015**, *524*, 69.

[13] T. Moorsom, M. Wheeler, T. Mohd Khan, F. Al Ma'Mari, C. Kinane, S. Langridge, D. Ciudad, A. Bedoya-Pinto, L. Hueso, G. Teobaldi, V. K. Lazarov, D. Gilks, G. Burnell, B. J. Hickey, O. Cespedes, *Phys. Rev. B* **2014**, *90*, 125311.
[14] A. Droghetti, S. Steil, N. Großmann, N. Haag, H. Zhang, M. Willis, W. P. Gillin, A. J. Drew, M. Aeschlimann, S. Sanvito, M. Cinchetti, *Phys. Rev. B* **2014**, *89*, 094412.
[15] E. C. Stoner, *Proc. R. Soc. London., Ser. A* **1938**, *165*, 372.
[16] U. von Barth, L. Hedin, *J. Phys. C: Solid State Phys.* **1972**, *5*, 1629.
[17] S. H. Vosko, L. Wilk, M. Nusair, *Can. J. Phys.* **1980**, *58*, 1200.
[18] R. Zeller, in *Computational Nanoscience: Do It Yourself!,* NIC Series, Vol. *31* (Eds: J. Grotendorst, S. Blügel, D. Marx), John von Neumann Institute for Computing, Jülich, Germany **2006**, p. 419.
[19] A. I. Lichtenstein, M. I. Katsnelson, G. Kotliar, *Phys. Rev. Lett.* **2001**, *87*, 67205.
[20] R. Gotter, A. Verna, M. Sbroscia, R. Moroni, F. Bisio, S. Iacobucci, F. Offi, S. R. Vaidya, A. Ruocco, G. Stefani, *Phys. Rev. Lett.* **2020**, *125*, 067202.
[21] M. M. Steiner, R. C. Albers, L. J. Sham, *Phys. Rev. B* **1992**, *45*, 13272.
[22] J. Sánchez-Barriga, J. Fink, V. Boni, I. Di Marco, J. Braun, J. Minár, A. Varykhalov, O. Rader, V. Bellini, F. Manghi, H. Ebert, M. I. Katsnelson, A. I. Lichtenstein, O. Eriksson, W. Eberhardt, H. A. Dürr, *Phys. Rev. Lett.* **2009**, *103*, 267203.
[23] J. Minár, J. Braun, H. Ebert, *J. Electron Spectrosc. Relat. Phenom.* **2013**, *189*, 129.
[24] D. E. Eastman, F. J. Himpsel, J. A. Knapp, *Phys. Rev. Lett.* **1978**, *40*, 1514.
[25] A. Liebsch, *Phys. Rev. Lett.* **1979**, *43*, 1431.
[26] S. Monastra, F. Manghi, C. A. Rozzi, C. Arcangeli, E. Wetli, H.-J. Neff, T. Greber, J. Osterwalder, *Phys. Rev. Lett.* **2002**, *88*, 236402.
[27] J. Braun, J. Minár, H. Ebert, M. I. Katsnelson, A. I. Lichtenstein, *Phys. Rev. Lett.* **2006**, *97*, 227601.
[28] L. Chioncel, C. Morari, A. Östlin, W. H. Appelt, A. Droghetti, M. M. Radonjić, I. Rungger, L. Vitos, U. Eckern, A. V. Postnikov, *Phys. Rev. B* **2015**, *92*, 054431.
[29] L. Sponza, P. Pisanti, A. Vishina, D. Pashov, C. Weber, M. van Schilf gaarde, S. Acharya, J. Vidal, G. Kotliar, *Phys. Rev. B* **2017**, *95*, 041112.
[30] C. Guillot, Y. Ballu, J. Paigné, J. Lecante, K. P. Jain, P. Thiry, R. Pinchaux, Y. Pétroff, L. M. Falicov, *Phys. Rev. Lett.* **1977**, *39*, 1632.
[31] M. Escher, N. B. Weber, M. Merkel, L. Plucinski, C. M. Schneider, *e-J. Surf. Sci. Nanotechnol.* **2011**, *9*, 340.
[32] S. Borek, J. Braun, J. Minár, H. Ebert, *Phys. Rev. B* **2015**, *92*, 075126.
[33] R. Bertacco, F. Ciccacci, *Phys. Rev. B* **1999**, *59*, 4207.
[34] K. Medjanik, O. Fedchenko, S. Chernov, D. Kutnyakhov, M. Ellguth, A. Oelsner, B. Schönhense, T. R. F. Peixoto, P. Lutz, C.-H. Min, F. Reinert, S. Däster, Y. Acremann, J. Viefhaus, W. Wurth, H. J. Elmers, G. Schönhense, *Nat. Mater.* **2017**, *16*, 615.
[35] B. Hammer, J. K. Norskov, *Nature* **1995**, *376*, 238.
[36] J. K. Norsko, *Rep. Prog. Phys.* **1990**, *53*, 1253.
[37] B. Hammer, J. K. Nørskov, *Surf. Sci.* **1995**, *343*, 211.
[38] D. M. Newns, *Phys. Rev.* **1969**, *178*, 1123.
[39] S. Bhattacharjee, U. V. Waghmare, S. C. Lee, *Sci. Rep.* **2016**, *6*, 35916.
[40] A. Droghetti, M. M. Radonjić, A. Halder, I. Rungger, L. Chioncel, *Phys. Rev. B* **2022**, *105*, 115129.
[41] G. Kotliar, S. Y. Savrasov, K. Haule, V. S. Oudovenko, O. Parcollet, C. A. Marianetti, *Rev. Mod. Phys.* **2006**, *78*, 865.
[42] A. Droghetti, M. M. Radonjić, L. Chioncel, I. Rungger, *Phys. Rev. B* **2022**, *106*, 075156.
[43] A. Grechnev, I. Di Marco, M. I. Katsnelson, A. I. Lichtenstein, J. Wills, O. Eriksson, *Phys. Rev. B* **2007**, *76*, 035107.
[44] J. Callaway, C. S. Wang, *Phys. Rev. B* **1977**, *16*, 2095.
[45] E. Młyńczak, M. C. T. D. Müller, P. Gospodarič, T. Heider, I. Aguilera, G. Bihlmayer, M. Gehlmann, M. Jugovac, G. Zamborlini, C. Tusche, S. Suga, V. Feyer, L. Plucinski, C. Friedrich, S. Blügel, C. M. M. Schneider, *Nat. Commun.* **2019**, *10*, 505.
[46] E. Młyńczak, I. Aguilera, P. Gospodarič, T. Heider, M. Jugovac, G. Zamborlini, C. Tusche, S. Suga, V. Feyer, S. Blügel, L. Plucinski, C. M. Schneider, *Phys. Rev. B* **2021**, *103*, 035134.
[47] A. Tange, C. L. Gao, B. Y. Yavorsky, I. V. Maznichenko, C. Etz, A. Ernst, W. Hergert, I. Mertig, W. Wulfhekel, J. Kirschner, *Phys. Rev. B* **2010**, *81*, 195410.
[48] M. Zheng, E. F. Schwier, H. Iwasawa, K. Shimada, *Chin. Phys. B* **2020**, *29*, 067901.
[49] A. Clarke, N. B. Brookes, P. D. Johnson, M. Weinert, B. Sinković, N. V. Smith, *Phys. Rev. B* **1990**, *41*, 9659.
[50] M. Getzlaff, J. Bansmann, G. Schönhense, *Fresenius J Anal Chem* **1995**, *353*, 743.
[51] C. Tusche, M. Ellguth, V. Feyer, A. Krasyuk, C. Wiemann, J. Henk, C. M. Schneider, J. Kirschner, *Nat. Commun.* **2018**, *9*, 3727.
[52] P. D. Johnson, A. Clarke, N. B. Brookes, S. L. Hulbert, B. Sinkovic, N. V. Smith, *Phys. Rev. Lett.* **1988**, *61*, 2257.
[53] A. Droghetti, P. Thielen, I. Rungger, N. Haag, N. Großmann, J. Stöckl, B. Stadtmüller, M. Aeschlimann, S. Sanvito, M. Cinchetti, *Nat. Commun.* **2016**, *7*, 12668.
[54] A. Vojvodic, J. K. Nørskov, F. Abild-Pedersen, *Top. Catal.* **2014**, *57*, 25.
[55] A. Picone, G. Fratesi, A. Brambilla, P. Sessi, F. Donati, S. Achilli, L. Maini, M. I. Trioni, C. S. Casari, M. Passoni, A. Li Bassi, M. Finazzi, L. Duò, F. Ciccacci, *Phys. Rev. B* **2010**, *81*, 115450.
[56] C. Tusche, M. Ellguth, A. A. Ünal, C. T. Chiang, A. Winkelmann, A. Krasyuk, M. Hahn, G. Schönhense, J. Kirschner, *Appl. Phys. Lett.* **2011**, *99*, 032505.
[57] C. Tusche, M. Ellguth, A. Krasyuk, A. Winkelmann, D. Kutnyakhov, P. Lushchyk, K. Medjanik, G. Schönhense, J. Kirschner, *Ultramicroscopy* **2013**, *130*, 70.
[58] A. R. Rocha, V. M. García-Suárez, S. Bailey, C. Lambert, J. Ferrer, S. Sanvito, *Phys. Rev. B* **2006**, *73*, 085414.
[59] I. Rungger, A. Droghetti, M. Stamenova, in *Handbook of Materials Modeling* (Eds: W. Andreoni, S. Yip) Springer, Cham, Switzerland **2020**, pp. 957–983.
[60] J. M. Soler, E. Artacho, J. D. Gale, A. García, J. Junquera, P. Ordejón, D. Sánchez-Portal, *J. Phys., Condens. Matter* **2002**, *14*, 2745.
[61] I. Rungger, S. Sanvito, *Phys. Rev. B: Condens. Matter Mater. Phys.* **2008**, *78*, 035407.
[62] A. Droghetti, I. Rungger, *Phys. Rev. B* **2017**, *95*, 085131.
[63] M. Imada, A. Fujimori, Y. Tokura, *Rev. Mod. Phys.* **1998**, *70*, 1039.
[64] V. I. Anisimov, O. Gunnarsson, *Phys. Rev. B* **1991**, *43*, 7570.